Enhancing Light-Driven Production of Hydrogen Peroxide by Anchoring Au onto C_3N_4 Catalysts

Xiaoyu Chang [1], Junjiao Yang [1], Dandan Han [1], Bing Zhang [2], Xu Xiang [1,]* and Jing He [1]

[1] State Key Laboratory of Chemical Resource Engineering, Beijing University of Chemical Technology, Beijing 100029, China; m15613731082@163.com (X.C.); yangjj@mail.buct.edu.cn (J.Y.); qing123yuan@126.com (D.H.); jinghe@263.net.cn (J.H.)

[2] School of Chemical Engineering, Zhengzhou University, Zhengzhou 450001, China; zhangb@zzu.edu.cn

* Correspondence: xiangxu@mail.buct.edu.cn; Tel.: +86-10-6443-2931

check for updates

Abstract: Light-driven production of hydrogen peroxide (H_2O_2) is a green and sustainable way to achieve solar-to-chemical energy conversion. During such a conversion, both the high activity and the stability of catalysts were critical. We prepared an Au-supported C_3N_4 catalyst—i.e., Au/C_3N_4-500(N_2)—by strongly anchoring Au nanoparticles (~5 nm) onto a C_3N_4 matrix—which simultaneously enhanced the activity towards the photosynthesis of H_2O_2 and the stability when it was reused. The yield of H_2O_2 reached 1320 μmol L^{-1} on Au/C_3N_4-500(N_2) after 4 h of light irradiation in an acidic solution (pH 3), which was higher than that (1067 μmol L^{-1}) of the control sample Au/C_3N_4-500(Air) and 2.3 times higher than that of the pristine C_3N_4. Particularly, the catalyst Au/C_3N_4-500(N_2) retained a much higher stability. The yield of H_2O_2 had a marginal decrease on the spent catalyst—i.e., 98% yield was kept. In comparison, only 70% yield was obtained from the spent control catalyst. The robust anchoring of Au onto C_3N_4 improved their interaction, which remarkably decreased the Au leaching when it was used and avoided the aggregation and aging of Au particles. Minimal Au leaching was detected on the spent catalyst. The kinetic analyses indicated that the highest formation rate of H_2O_2 was achieved on the Au/C_3N_4-500(N_2) catalyst. The decomposition tests and kinetic behaviors of H_2O_2 were also carried out. These findings suggested that the formation rate of H_2O_2 could be a determining factor for efficient production of H_2O_2.

Keywords: hydrogen peroxide; Au catalyst; photosynthesis; carbon nitride

1. Introduction

Hydrogen peroxide (H_2O_2)—a mild and environment-friendly oxidant—has been used as a green chemical and applied in a variety of industrial and living activities—such as papermaking, water treatment, chemical synthesis, disinfection, and sterilization [1]. In addition, H_2O_2 is a promising liquid fuel for H_2O_2-based fuel cells, because only water is emitted [2]. Compared with the widely known fuel H_2, H_2O_2 is easier to store and is more conveniently transported with a low risk of wastage. The current industrial production of H_2O_2 is based on an anthraquinone method. The advantages of this are a scale-up and high productivity of H_2O_2. However, huge energy consumption, complicated by-products, and safety issues are still challenges being faced. It is highly desirable to pursue an efficient, mild, and sustained method as an alternative for the synthesis of H_2O_2.

The light-driven formation of H_2O_2 has received increased attention in recent decades [3–8]. The process involves light capture on the photocatalyst, charge separation under light irradiation, charge transfer to the surface of the photocatalyst, water/alcohol oxidation by photo-generated holes, and the reduction of dioxygen by photo-generated electrons [9–11]. In such a process, a highly efficient photocatalyst could be a core factor in order to direct the synthesis of H_2O_2. Titanium dioxide (TiO_2),

a widely studied photocatalyst, has been found to enable the formation of H_2O_2 [12–16]. Several strategies have been developed to enhance the H_2O_2 yield on TiO_2-based photocatalysts. For example, the surface modification of TiO_2 by fluorine ions was proposed [13]. The loading of noble metal (Au) and alloys (AuAg) on TiO_2 were studied [14,16]. However, the robust hole oxidative capability of TiO_2 accelerated the decomposition of H_2O_2 on the surface of TiO_2, and thus lowered the H_2O_2 yield [17]. Additionally, the ultraviolet (UV) responsive characteristic of TiO_2 limited its light absorption and utilization. The graphitic phase carbon nitride (g-C_3N_4)—a polymeric layered material—was explored as a photocatalyst for pollutant decomposition and water splitting, because of its relatively narrow bandgap (~2.7 eV), and its suitable valence band and conduction band levels [18,19]. Recently, C_3N_4-based materials have been utilized in the light synthesis of H_2O_2 [20–25]. For instance, Shiraishi et al. reported the selective production of H_2O_2 on g-C_3N_4 photocatalyst [20]. The H_2O_2 production from water and molecular oxygen was improved on a pyromellitic diimide (PDI)-modified C_3N_4—by the same authors [21]. The modification caused the conduction and valence band levels of C_3N_4 to positively shift, which was more favorable to the two-electron reduction of dioxygen needed to produce H_2O_2. The mesoporous g-C_3N_4 was also prepared by using silica sol as a soft template [22]. The effects of surface defects on photocatalytic H_2O_2 production were also investigated. The results indicated that the suitably large surface area favored an increased H_2O_2 yield. Recently, a carbon nitride-aromatic diimide-graphene nanohybrid was synthesized which demonstrated extremely high activity towards H_2O_2 generation—possessing a solar-to-hydrogen peroxide conversion efficiency of 0.2% [24]. Furthermore, Moon et al. reported a photochemical production of H_2O_2 over carbon nitride frameworks incorporated with multiple heteroelements (K, P, and O) [25].

In our previous studies, the g-C_3N_4 exhibited enhanced activity when combined with mixed-metal oxide (MMO) [26]. The reason for this is that the positive shift of the conduction band of C_3N_4 improved the two-electron reduction of dioxygen to H_2O_2. Additionally, the MMO plays the role of the water oxidation catalyst (WOC), which has been recognized to be active in oxygen-evolving reactions [27–29]. Furthermore, the H_2O_2 production was increased on the carbon-modified g-C_3N_4, which regulates the energy levels and is more suitable for the selective two-electron reduction of oxygen by photo-generated electrons [30]. Consequently, the efficient separation of photo-excited electrons and holes, and appropriate band positions are advantageous to the production of H_2O_2. The noble metals (e.g., Au, Ag, and Pt) revealed the reductive ability in supported catalysts by collecting electrons, similar to a reservoir. The activity is closely related to the size of the noble metal nanoparticles. Generally, when the size of the metal particles is greater than 7 nm, the activity drops sharply [31]. However, the smaller-sized metal particles possess a low Tammann temperature and high surface energy, leading to low thermal stability and the sintering phenomenon when heated [32]. In this article, we investigated Au-supported C_3N_4 prepared by a stabilized method. The Au/C_3N_4 catalyst exhibited high activity towards H_2O_2 production and superior stability when reused. The strong anchoring of Au nanoparticles (around 5 nm) on C_3N_4 inhibited the leaching and prevented the particles from agglomerating in the sintering process of the catalyst. The kinetics were also studied in order to understand the determining pathway for H_2O_2 production.

2. Results

2.1. Catalyst Characterization

The Au loading and distribution on the C_3N_4 matrix were observed by transmission electron microscopy TEM (Figure 1). The average size of Au particles was 5.0 nm (Figure 1a,b) and 7.5 nm (Figure 1d,e) in the Au/C_3N_4-500(N_2) and Au/C_3N_4-500(Air) catalysts, respectively. The Au particles had a narrower size distribution on the Au/C_3N_4-500(N_2) than on the Au/C_3N_4-500(Air). The high-resolution transmission electron microscopy photographs showed that the distance of the neighboring planes was 0.235 nm in both catalysts, corresponding to the d-spacing of the plane (111) in Au [32]. Au particles had more crystal defects on the Au/C_3N_4-500(N_2) (Figure 1c) than on

the Au/C_3N_4-500(Air) (Figure 1f). The smaller-sized Au possessed more edges, corners, and steps, which were favorable for the adsorption of reactive species and further catalytic reactions. The energy dispersive spectrometer EDS mapping of the Au/C_3N_4-500(N_2) is presented in Figure 1g. The results suggested that Au, C, and N elements had a homogeneous distribution in the catalyst.
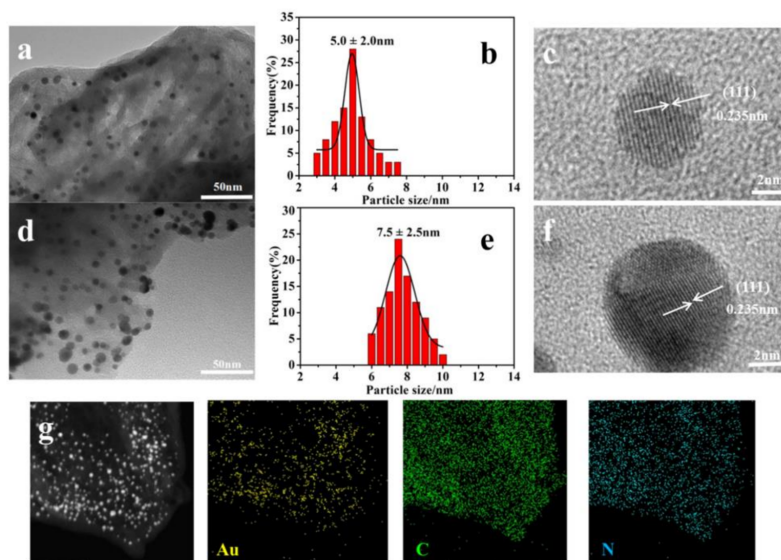

Figure 1. (**a**) TEM image; (**b**) particle size distribution and (**c**) HRTEM photograph of Au/C_3N_4-500(N_2); (**d**) TEM image; (**e**) particle size distribution and (**f**) HRTEM image of Au/C_3N_4-500(Air); (**g**) EDS mapping of Au/C_3N_4-500(N_2) (scale bar 100 nm). The elemental mappings show the distribution of Au, C, and N elements.

The phase structure of the catalysts was determined by X-ray diffractometer XRD (Figure 2). The diffractions at 2θ = 13.3° and 27.4° were indexed to the planes—namely, 100 and 002—of g-C_3N_4 (JCPDS 87-1526) in all samples, which originated from the in-plane repetition of tri-s-triazine and the stacking of the conjugated aromatic units, respectively [33]. The formation of Au was verified in the XRD patterns of the supported catalysts, in which the diffractions were indexed to the planes—namely, 111, 200, and 220 (JCPDS 04-0784) [34]. The loading of Au was estimated by Thermogravimetric analysis (TGA). The weight of Au was 1.05% and 1.35% in Au/C_3N_4-500(N_2) and Au/C_3N_4-500(Air), respectively (Figure S1). This indicated that the loading of Au in the two catalysts had minimal difference.
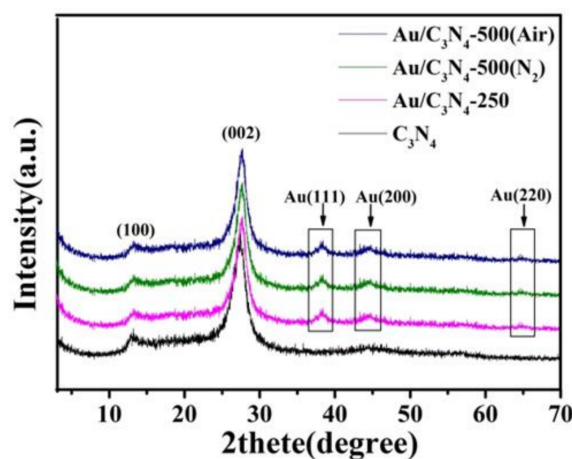

Figure 2. XRD patterns of C_3N_4, Au/C_3N_4-250, Au/C_3N_4-500(N_2), and Au/C_3N_4-500(Air).

The elemental valences and surface species were analyzed by X-ray photoelectron spectroscopy XPS (Figure 3), because of its surface-sensitive technique with a detection depth of less than ten nanometers. Two deconvoluted peaks, at 83.7 and 87.4 eV, were observed in the core level spectra of Au4f in Au/C_3N_4-500(N_2), which were assigned to zerovalent Au [35,36]. The peaks showed a slight shift (0.2 eV) towards decreased binding energy in that of Au/C_3N_4-500(Air) (Table 1). In both catalysts, the N1s core level spectra could be deconvoluted into three peaks. In the g-C_3N_4 phase, the peaks at 400.6, 399.2, and 398.5 eV corresponded to N-$(C)_3$, =N-, and C_2NH species, respectively [37,38]. The binding energy of the three peaks had a slight shift (<0.2 eV) between the Au/C_3N_4-500(N_2) and Au/C_3N_4-500(Air), which suggested that the nitrogen species had minimal change in both catalysts.
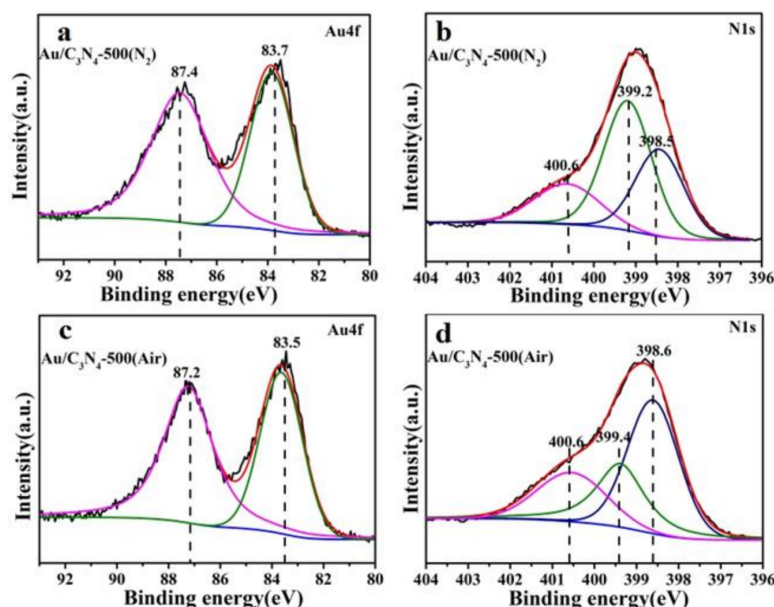

Figure 3. XPS core level spectra of (**a**) Au4f in Au/C_3N_4-500(N_2); (**b**) N1s in Au/C_3N_4-500(N_2) and (**c**) Au4f in Au/C_3N_4-500(Air); (**d**) N1s in Au/C_3N_4-500(Air).

Table 1. XPS binding energy of Au4f and N1s in the Au-supported C_3N_4 catalysts.

Catalysts	Au4f/eV		N1s/eV		
	4f$_{5/2}$	4f$_{7/2}$	N-$(C)_3$	=N-	C_2NH
Au/C_3N_4-500(N_2)	87.4	83.7	400.6	399.2	398.5
Au/C_3N_4-500(N_2)-reused	87.3	83.6	400.6	399.2	398.5
Au/C_3N_4-500(Air)	87.2	83.5	400.6	399.4	398.6
Au/C_3N_4-500(Air)-reused	87.0	83.3	400.6	399.4	398.6

The optical absorption properties of the supported catalysts were characterized by UV-visible diffuse reflectance spectra (Figure 4a). These spectra were obtained by converting the reflection data that was measured using the Kubelka–Munk equation: $F(R) = (1 − R)^2/2R$, where R is the reflectance [39]. The three Au/C_3N_4 samples showed enhanced absorption in both the UV and visible regions when compared with the bare C_3N_4. The absorption band below 400 nm in the UV region corresponded to the π–π* electron transition of the aromatic 1-, 3-, and 5-triazine compounds [40–42]. The localized surface plasmon resonance (LSPR) absorption of Au was apparent, peaking at ~550 nm in the Au/C_3N_4-250 and Au/C_3N_4-500(Air) samples. The Au/C_3N_4-500(N_2) sample presented more intensive absorption throughout the spectral region measured. This suggested that the metal–support interaction differed between the Au/C_3N_4-500(N_2) and Au/C_3N_4-500(Air), which could have affected the photocatalytic properties. The fluorescence spectra were measured because the fluorescence emission properties were associated with the carrier recombination (Figure 4b). The C_3N_4 itself

exhibited an emission band that peaked at 462 nm, which was attributed to the transition between the lone pair valence band and the π^* conduction band in the framework of graphitic C_3N_4 [43]. After the loading of Au nanoparticles, the intensity of the emission band decreased significantly in the Au/C_3N_4-250 and Au/C_3N_4-500(Air). Notably, the emission in the Au/C_3N_4-500(N_2) was almost quenched. The quenching of fluorescence emission indicated the suppression of carrier recombination under photo-excitation. The efficient blockage of the recombination channel could have favored the carrier separation and thus stimulated the electrons and holes to involve the photocatalytic reactions on the surface of catalysts. The reduction of emission intensity was more significant in the Au/C_3N_4-500(N_2) than in the Au/C_3N_4-500(Air). It could have indicated that the metal–support interaction was more intensive in the former, which was beneficial for the feasible electron transfer of photo-excited C_3N_4 to Au.
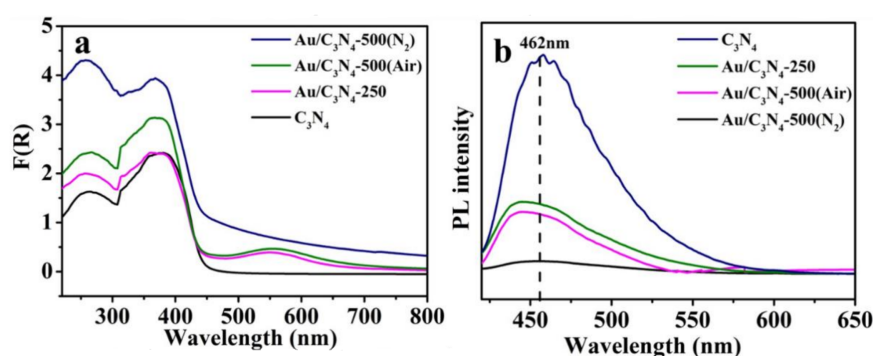

Figure 4. (**a**) Ultraviolet (UV)/Visible diffuse reflectance spectra; (**b**) fluorescence emission spectra of C_3N_4, Au/C_3N_4-250, Au/C_3N_4-500(Air), and Au/C_3N_4-500(N_2); across an excitation wavelength of 400 nm.

2.2. Photosynthesis of H_2O_2

The photocatalytic generation of H_2O_2 on the catalysts was conducted in an O_2-equilibrated acidic aqueous solution (pH 3) under light irradiation. The H_2O_2 yield is shown (Figure 5a) as a function of time. The yield increased with time on all catalysts. The higher yield was observed on the Au/C_3N_4-500(N_2) from the beginning of the reactions. After 240 min of irradiation, the H_2O_2 yield reached 1320 and 1067 μmol L^{-1} on the Au/C_3N_4-500(N_2) and Au/C_3N_4-500(Air), respectively—both of which were higher than that on the C_3N_4 (582 μmol L^{-1}) (Table 2). The yield was higher for the Au/C_3N_4-500(N_2) than for the Au/C_3N_4-500(Air), although the latter had a larger Au loading—1.05% wt in Au/C_3N_4-500(N_2) and 1.35% wt in Au/C_3N_4-500(Air) catalyst. We concluded that the catalytic activity of Au/C_3N_4-500(N_2) was higher than that of Au/C_3N_4-500(Air). This was potentially ascribed to the smaller size of Au nanoparticles in the Au/C_3N_4-500(N_2) (Figure 1). Similar findings were also observed in the Au- and AuAg-loaded TiO_2 photocatalytsts [14,16]. The apparent quantum yield (Φ_{AQY}) for H_2O_2 formation over the Au/C_3N_4-500(N_2) was calculated using the equation Φ_{AQY} (%) = (2 × [H_2O_2] formed)/(photon number entered into the reaction vessel) × 100. The Φ_{AQY} value measured at a monochromic light of 400 nm was 3.63% (see Supplementary Materials for details).

In order to understand the effect of the light wavelength irradiated, we measured the H_2O_2 generation under light irradiation with a cut-off filter of 420 nm (Figure S2). After 4 h of irradiation, the H_2O_2 yield reached 694 μmol L^{-1} under the cut-off filter of 420 nm, lower than that measured without the cut-off filter on the Au/C_3N_4-500(N_2) (1320 μmol L^{-1}). This suggested that the irradiation of UV light contributed to the formation of H_2O_2 when no cut-off filter was used. This indicated that the UV irradiation possessed high energy and could stimulate the C_3N_4 (with a bandgap of ~2.8 eV) to generate photo-carriers. The Au nanoparticles showed the LSPR absorption band at around 550 nm. As a result, the Au/C_3N_4-500(N_2) had intensive absorption above 500 nm, while the C_3N_4 showed minimal absorption in the same spectral region (>500 nm) (Figure 4a). To understand the effect of LSPR

on the production of H_2O_2, we used a cut-off filter of 510 nm. The H_2O_2 yield was 10 times higher for the Au/C_3N_4-500(N_2) (293 µmol L^{-1}) than for the C_3N_4 (25 µmol L^{-1}) after 4 h of irradiation (Figure S3). The LSPR of Au enhanced light absorption around the plasmon resonance band and contributed considerably to H_2O_2 production. To compare the effect of Au loading on the activity, we prepared another two samples of Au/C_3N_4-500(N_2), with an Au loading of 1% and 3% (a nominal weight). The H_2O_2 production was carried out on the two catalysts under the same reaction conditions. The H_2O_2 yield after 4 h of irradiation was 743, 1320, and 917 µmol L^{-1}, on 1%, 2%, and 3% Au-supported catalysts, respectively (Figure S4). This finding indicated that an appropriate Au loading led to a higher H_2O_2 yield. Higher Au loading might have caused larger-sized Au particles and the reduction in activity [44,45]. The Au/C_3N_4-500(N_2) catalyst was prepared by a carbon-layer-stabilized method, where the dopamine molecule was used as a precursor of the carbon layer. In order to show the effect of dopamine, we prepared a control sample without a treatment of dopamine and named it Au/C_3N_4-500(N_2)-without dopa. The H_2O_2 yield after 4 h of irradiation was 1320 and 1065 µmol L^{-1} on the Au/C_3N_4-500(N_2) and Au/C_3N_4-500(N_2)-without dopa, respectively (Figure S5). This finding verified the effect of dopamine on the activity of the catalyst.

The H_2O_2 concentration–time data (Figure 5a) was fitted using the equation $[H_2O_2] = (K_f/K_d)$ $\{1-exp(-K_dt)\}$, where K_f and K_d were the formation and decomposition rate constants of H_2O_2, respectively, and t was the irradiation time [4,26]. The solid lines (Figure 5a) were the fitted curves. Based on the fitted results (Figure S6), the K_f and K_d values were listed (Table 2) and plotted (Figure 5b). Both K_f and K_d values were the smallest on the C_3N_4. The K_f value was the largest on the Au/C_3N_4-500(N_2) (7.893 µmol L^{-1} min^{-1}) and the K_d value was smaller on the Au/C_3N_4-500(N_2) than on the Au/C_3N_4-500(Air) (0.00354 vs. 0.00446 min^{-1}). This indicated that a larger K_f value and smaller K_d value led to a higher yield of H_2O_2. The formation rate of H_2O_2 was dominant in the process of H_2O_2 production. This was consistent with our previous studies on the metal oxide@C_3N_4 and carbon-doped C_3N_4 catalysts [26,30].
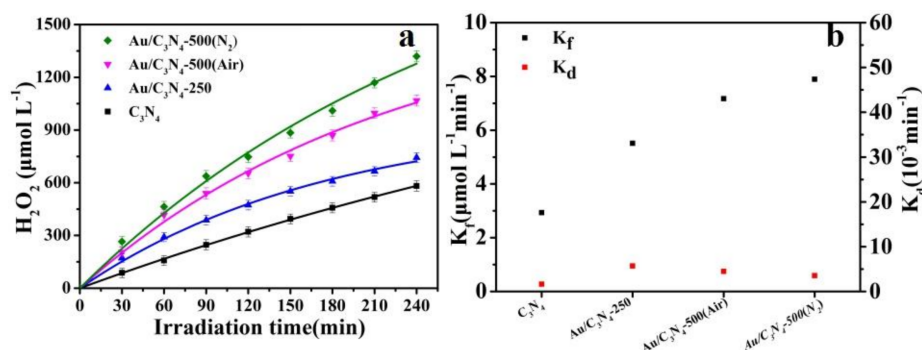

Figure 5. (**a**) The light-driven hydrogen peroxide (H_2O_2) generation in an O_2-equilibrated aqueous solution over C_3N_4, Au/C_3N_4-250, Au/C_3N_4-500(Air), and Au/C_3N_4-500(N_2). The experimental conditions: 1 g/L of photocatalyst, pH 3.0, 5% vol of 2-propanol, Xe lamp, illumination intensity of 100 mW/cm^2; and (**b**) formation rate constant (K_f) and decomposition rate constant (K_d) for H_2O_2 production.

Table 2. The yield of hydrogen peroxide (H_2O_2) and the kinetic analyses.

Sample	H_2O_2 Yield at 120 min (µmol L^{-1})	H_2O_2 Yield at 240 min (µmol L^{-1})	K_f (µmol L^{-1} min^{-1})	K_d (10^{-3} min^{-1})
C_3N_4	321	582	2.929	1.61
Au/C_3N_4-250	473	743	5.514	5.68
Au/C_3N_4-500(Air)	653	1067	7.170	4.46
Au/C_3N_4-500(N_2)	747	1320	7.893	3.54

The decomposition behaviors of H_2O_2 on the catalysts were further investigated under an excessive amount of H_2O_2 (initial concentration of H_2O_2 of 5 mM) (Figure 6). The decomposition data was fitted using a pseudo-first-order equation: $-dC(t)/dt = kt$, where $C(t)$ is the H_2O_2 concentration at certain a time, k is the decomposition rate constant, and t is the time. The fitted results showed that the decomposition rate constant followed the order of Au/C_3N_4-500(N_2) (0.00406 min^{-1}) > Au/C_3N_4-500(Air) (0.00251 min^{-1}) > Au/C_3N_4-250 (0.00181 min^{-1}) > C_3N_4 (0.00097 min^{-1}) (Figure S7). The k values had the same order of magnitude as those in the production of H_2O_2 (Table 2). The decomposition of H_2O_2 on the Au-loaded C_3N_4 catalysts was less dependent on the concentration of H_2O_2. The sustained production of H_2O_2 was mainly dominated by its formation rate.
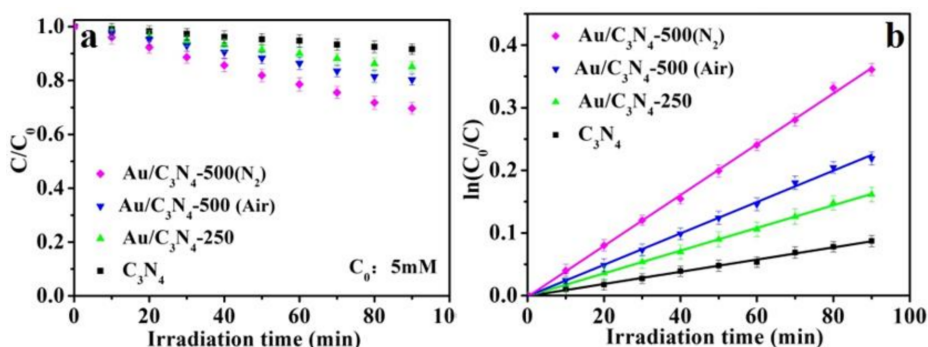

Figure 6. The photocatalytic decomposition of H_2O_2 (C_0 = 5 mM) on the C_3N_4, Au/C_3N_4-250, Au/C_3N_4-500(Air), and Au/C_3N_4-500(N_2). (**a**) The changes of C/C_0 with irradiation time; (**b**) The changes of $\ln(C/C_0)$ with irradiation time. The experimental conditions: 1 g/L of photocatalyst, pH 3.0, Xe lamp, and illumination intensity of 100 mW/cm^2.

2.3. Stability of the Photocatalysts

The stable production of H_2O_2 was required on the spent catalysts. After being used for the photosynthesis of H_2O_2, the catalysts were separated from the solution and recycled for reuse. We studied the repeated use of the Au/C_3N_4 catalysts to confirm their stability. The H_2O_2 yield was almost the same on the spent Au/C_3N_4-500(N_2) as on the original Au/C_3N_4-500(N_2), having a negligible decrease of less than 2% (Figure 7). However, the H_2O_2 yield showed a significant reduction on the reused Au/C_3N_4-500(Air) and only 70% of the original yield was retained. This suggested that Au/C_3N_4-500(N_2) had a much higher stability than Au/C_3N_4-500(Air) for the photosynthesis of H_2O_2. This was verified by the structural characterizations of the spent catalysts.
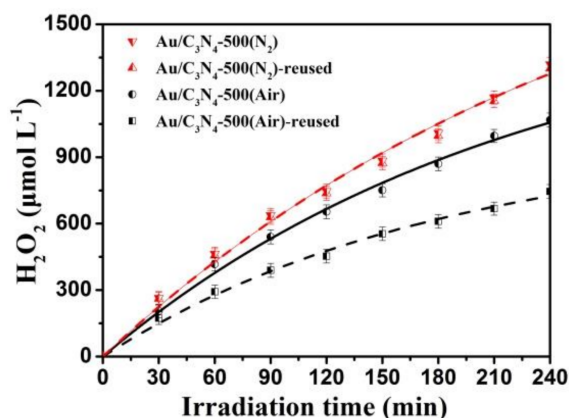

Figure 7. The repeated use of Au/C_3N_4-500(N_2) and Au/C_3N_4-500(Air) for H_2O_2 generation. The experimental conditions: 1 g/L of photocatalyst, pH 3.0, 5% vol of 2-propanol, Xe lamp, illumination intensity of 100 mW/cm^2, and O_2-equilibrated conditions.

The spent catalysts were characterized by TEM, inductively-coupled plasma spectrum ICP, and XPS. The average size of Au particles increased from 5 to 7 nm in the Au/C_3N_4-500(N_2) after reactions (Figure 8a,b). The Au particles had less agglomeration and were still highly dispersed in the C_3N_4 matrix. In contrast, the Au particles showed an increase in size from 7.5 to 10 nm in the Au/C_3N_4-500(Air) (Figure 8c,d). The Au particles exhibited obvious aggregates. In addition, the elemental analyses showed that the Au loading had a slight loss of 5.7% in the spent Au/C_3N_4-500(N_2), while the Au remarkably lost 17.8% in the spent Au/C_3N_4-500(Air) (Figure S1). Such a significant leaching of Au could be a critical factor for the sharp decrease of H_2O_2 yield, as well as the increased size of Au particles in Au/C_3N_4-500(Air) (Figure 7). The XPS results indicated that the valence of Au had no change and Au still existed in the form of zero-valence. The fitted peaks in the N1s spectra had minimal shift compared to the original catalysts (Figure S8).
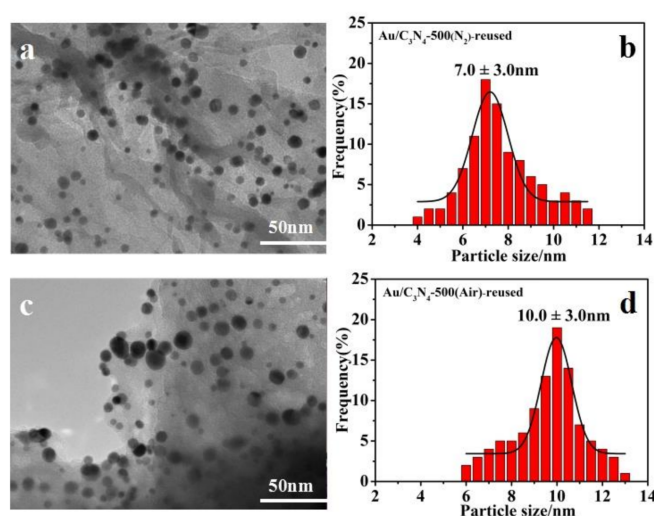

Figure 8. (**a**) TEM images and (**b**) particle-size distribution of Au/C_3N_4-500(N_2)-reused; (**c**) TEM images and (**d**) particle-size distribution of Au/C_3N_4-500(Air)-reused.

The flatband potentials (E_{fb}) of the catalysts were estimated from the electrochemical Mott–Schottky plots, measured at varied frequencies. The Mott–Schottky plots exhibited positive slopes, characteristic of n-type semiconductors (Figure 9) [26]. The E_{fb} values were derived by extrapolating the plots to the *x*-axis, which were −0.86 V, −0.68 V, and −0.70 V (vs. RHE) for C_3N_4, Au/C_3N_4-500(N_2), and Au/C_3N_4-500(Air), respectively. The E_{fb} values of Au-supported C_3N_4 catalysts had a minimal positive shift (~0.16 V) compared with that of C_3N_4, and had minimal difference between Au/C_3N_4-500(N_2) and Au/C_3N_4-500(Air). Generally, the conduction band potential was approximately equal to the E_{fb} [30]. Consequently, the conduction band levels hardly changed in the Au-supported catalysts, regardless of the stability. The bandgap of the catalysts was also determined from the Tauc plots. The Tauc plots of Au/C_3N_4-500(N_2) and Au/C_3N_4-500(Air) were derived according to the equation $(F(R) \cdot h\upsilon)^2 = A(h\upsilon-E_g)$, where h was Plank constant, υ was the frequency, A was a constant, and E_g was the band gap (Figure S9) [39,46,47]. The estimated bandgap was 2.83 eV and 2.85 eV for the Au/C_3N_4-500(N_2) and Au/C_3N_4-500(Air), respectively. Additionally, the bandgap values had no change in the spent catalysts. From the energy level analyses, we concluded that the different activity and stability of the Au-supported C_3N_4 catalysts were mainly affected by the Au sizes and metal–support interactions rather than the energy band structure.
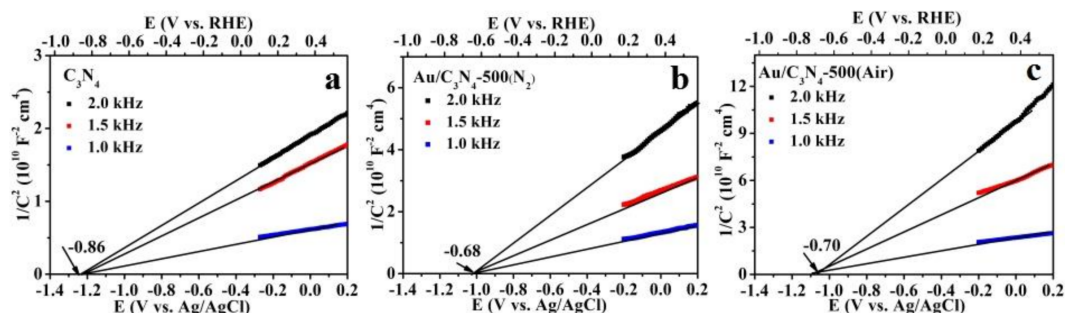
Figure 9. Mott–Schottky plots of (**a**) C_3N_4, (**b**) Au/C_3N_4-500(N_2), and (**c**) Au/C_3N_4-500(Air) in an acidic solution (pH 3) in the dark. The frequency used was 1.0 kHz, 1.5 kHz, and 2.0 kHz.

3. Materials and Methods

3.1. Materials

Melamine, isopropanol, and $HClO_4$ were purchased from Sinopharm Chemical Reagent (Beijing Co. Ltd., Beijing, China). $HAuCl_4 \cdot 3H_2O$ was purchased from Shanghai Aladdin Biochemical Technology Co. Ltd. (Beijing, China) KH_2PO_4, $K_2HPO_4 \cdot 3H_2O$, H_2SO_4 (98%), and H_2O_2 (30%) were purchased from Beijing Chemical Reagent Co. Ltd. (Beijing, China).Peroxidase was purchased from Beijing Lamboride Trading Company (Beijing, China). *N*-diethyl-1,4-phenylenediamine sulfate (99%) was purchased from Adamas Reagent Co. Ltd. (Beijing, China) O_2 (99.995%) was purchased from Hai Pu Gas Co. Ltd. (Beijing, China) All reagents were of analytical grade and were used without further purification. Deionized water was used throughout the experiments.

3.2. Catalyst Preparation

3.2.1. Preparation of g-C_3N_4

The g-C_3N_4 was prepared by heating of a melamine precursor [33]. The melamine (10 g) was added to a porcelain cup and calcined for 4 h at 520 °C (heating rate of 4 °C min^{-1}). The product was a yellow powder.

3.2.2. Synthesis of Au-Supported C_3N_4 Catalysts

Au/C_3N_4-250 Catalyst

The Au/C_3N_4-250 catalyst was synthesized by a method similar to the literature [32]. Briefly, the pH value of an aqueous solution (0.02 g $HAuCl_4 \cdot 3H_2O$ in 60 mL water) was adjusted to 10.0 by adding 1 M NaOH. 1 g of C_3N_4 powder was added to the solution and heated to 70 °C for 2 h under stirring. The suspension was washed three times using deionized water by centrifugation. Finally, the product was dried for 2 h at 40 °C and subsequently calcined in air for 2 h at 250 °C. Before further use, the product was sealed in vacuum desiccator at room temperature.

Au/C_3N_4-500(N_2) Catalyst

Firstly, the Au/C_3N_4-250 sample was modified with dopamine according to the previous method [48]. The 0.5 g of Au/C_3N_4-250 powder was added to 1 mg mL^{-1} dopamine-containing solution, which was pre-adjusted to pH 8.5 by a tris-buffer solution (10 mM). The suspension was stirred for 24 h, allowing for the formation of polydopamine (PDA) on the surface of solid. Subsequently, the suspension was separated by centrifugation, washed three times using deionized water and once using ethanol. The product was dried for 2 h at 40 °C. Subsequently, the dried product was annealed in a gas flow of nitrogen for 2 h (heating rate of 5 °C min^{-1}) at 500 °C. The resulting powder was further annealed in air for 2 h at 500 °C to obtain the Au/C_3N_4-500(N_2) catalyst.

Au/C$_3$N$_4$-500(Air) Catalyst

The 0.5 g of Au/C$_3$N$_4$-250 powder was directly annealed in air for 2 h at 500 °C to obtain the Au/C$_3$N$_4$ -500(Air) catalyst.

4. Conclusions

The Au nanoparticles were strongly anchored onto the C$_3$N$_4$ matrix by a carbon-layer-stabilized method. The as-prepared Au/C$_3$N$_4$-500(N$_2$) catalyst showed higher activity towards light-driven synthesis of H$_2$O$_2$ than the control Au/C$_3$N$_4$-500(Air). This was ascribed to the smaller size of Au nanoparticles (~5 nm) and the stronger metal–support interaction on the Au/C$_3$N$_4$-500(N$_2$). The H$_2$O$_2$ yield reached 1320 μmol L^{-1} after 240 min of light irradiation in an acidic solution (pH 3), 2.3 times higher than that of the pristine C$_3$N$_4$. The spent Au/C$_3$N$_4$-500(N$_2$) catalyst exhibited a marginal loss of activity and the H$_2$O$_2$ yield remained >98% of the original yield. However, the H$_2$O$_2$ yield decreased to 70% of the original yield on the Au/C$_3$N$_4$-500(Air) catalyst when reused. There were primarily two reasons for this. One was the significant leaching of Au (17.8%) from the Au/C$_3$N$_4$-500(Air) catalyst after reactions, much greater than that (5.7%) from the Au/C$_3$N$_4$-500(N$_2$) catalyst. The other was the increased sizes of Au (~10 nm) on Au/C$_3$N$_4$-500(Air), which led to the decrease in activity. The energy band structures of the Au/C$_3$N$_4$-500(N$_2$) and the Au/C$_3$N$_4$-500(Air) showed minimal difference before or after the reactions. Therefore, the highly stable Au-supported C$_3$N$_4$ catalyst could be favorable for the sustained production of H$_2$O$_2$ via a two-electron reduction of dioxygen driven by solar light.

Author Contributions: Xu Xiang conceived and designed the experiments; Xiaoyu Chang and Dandan Han performed the experiments; Xu Xiang, Xiaoyu Chang, Jing He, Jun Jiao Yang, and Bing Zhang analyzed the data; Xu Xiang and Xiaoyu Chang wrote the manuscript.

Conflicts of Interest: The authors declare no conflict of interest.

References

1. Campos-Martin, J.M.; Blanco-Brieva, G.; Fierro, J.L.G. Hydrogen peroxide synthesis: An outlook beyond the anthraquinone process. *Angew. Chem. Int. Ed.* **2006**, *45*, 6962–6984. [CrossRef] [PubMed]
2. Kato, S.; Jung, J.; Suenobua, T.; Fukuzumi, S. Production of hydrogen peroxide as a sustainable solar fuel from water and dioxygen. *Energy Environ. Sci.* **2013**, *6*, 3756–3764. [CrossRef]
3. Isaka, Y.; Kato, S.; Hong, D.; Suenobu, T.; Yamada, Y.; Fukuzumi, S. Bottom-up and top-down methods to improve catalytic reactivity for photocatalytic production of hydrogen peroxide using a Ru-complex and water oxidation catalysts. *J. Mater. Chem. A* **2015**, *3*, 12404–12412. [CrossRef]
4. Isaka, Y.; Oyama, K.; Yamada, Y.; Suenobu, T.; Fukuzumi, S. Photocatalytic production of hydrogen peroxide from water and dioxygen using cyano-bridged polynuclear transition metal complexes as water oxidation catalysts. *Catal. Sci. Technol.* **2016**, *6*, 681–684. [CrossRef]
5. Thakur, S.; Kshetri, T.; Kim, N.H.; Lee, J.H. Sunlight-driven sustainable production of hydrogen peroxide using a CdS–graphene hybrid photocatalyst. *J. Catal.* **2017**, *345*, 78–86. [CrossRef]
6. Fukushima, M.; Tatsumi, K.; Tanaka, S.; Nakamura, H. Photocatalytic production of hydrogen peroxide by tris(2,2'-bipyridine) ruthenium(II) using humic acids as electron donor. *Environ. Sci. Technol.* **1998**, *32*, 3948–3953. [CrossRef]

7. Zhuang, H.; Yang, L.; Xu, J.; Li, F.; Zhang, Z.; Lin, H.; Long, J.; Wang, X. Robust photocatalytic H_2O_2 production by octahedral $Cd_3(C_3N_3S_3)_2$ coordination polymer under visible light. *Sci. Rep.* **2015**, *5*, 16947. [CrossRef] [PubMed]

8. Zhao, S.; Zhao, X.; Zhang, H.; Li, J.; Zhu, Y. Covalent combination of polyoxometalate and graphitic carbon nitride for light-driven hydrogen peroxide production. *Nano Energy* **2017**, *35*, 405–414. [CrossRef]

9. Yamada, Y.; Nomura, A.; Miyahigashi, T.; Ohkubo, K.; Fukuzumi, S. Acetate induced enhancement of photocatalytic hydrogen peroxide production from qxalic acid and dioxygen. *J. Phys. Chem. A* **2013**, *117*, 3751–3760. [CrossRef] [PubMed]

10. Aratani, Y.; Suenobu, T.; Ohkubo, K.; Yamada, Y.; Fukuzumi, S. Dual function photocatalysis of cyano-bridged heteronuclear metal complexes for water oxidation and two-electron reduction of dioxygen to produce hydrogen peroxide as a solar fuel. *Chem. Commun.* **2017**, *53*, 3473–3476. [CrossRef] [PubMed]

11. Isaka, Y.; Yamada, Y.; Suenobu, T.; Nakagawa, T.; Fukuzumi, S. Production of hydrogen peroxide by combination of semiconductor-photocatalysed oxidation of water and photocatalytic two-electron reduction of dioxygen. *RSC Adv.* **2016**, *6*, 42041–42044. [CrossRef]

12. Cai, R.; Kubota, Y.; Fujishima, A. Effect of copper ions on the formation of hydrogen peroxide from photocatalytic titanium dioxide particles. *J. Catal.* **2003**, *219*, 214–218. [CrossRef]

13. Maurino, V.; Minero, C.; Mariella, G.; Pelizzetti, E. Sustained production of H_2O_2 on irradiated TiO_2-fluoride systems. *Chem. Commun.* **2005**, *20*, 2627–2629. [CrossRef] [PubMed]

14. Tsukamoto, D.; Shiro, A.; Shiraishi, Y.; Shiraishi, Y.; Sugano, Y.; Ichikawa, S.; Tanaka, S.; Hirai, T. Photocatalytic H_2O_2 production from ethanol/O_2 system using TiO_2 loaded with Au-Ag bimetallic alloy nanoparticles. *ACS Catal.* **2012**, *2*, 599–603. [CrossRef]

15. Shiraishi, Y.; Kanazawa, S.; Tsukamoto, D.; Shiro, A.; Sugano, Y.; Hirai, T. Selective hydrogen peroxide formation by titanium dioxide photocatalysis with benzylic alcohols and molecular oxygen in water. *ACS Catal.* **2013**, *3*, 2222–2227. [CrossRef]

16. Teranishi, M.; Naya, S.; Tada, H. In situ liquid phase synthesis of hydrogen peroxide from molecular oxygen using gold nanoparticle-loaded titanium(IV) dioxide photocatalyst. *J. Am. Chem. Soc.* **2010**, *132*, 7850–7851. [CrossRef] [PubMed]

17. Li, X.; Chen, C.; Zhao, J. Mechanism of photodecomposition of H_2O_2 on TiO_2 surfaces under visible light irradiation. *Langmuir* **2001**, *17*, 4118–4122. [CrossRef]

18. Wang, X.; Maeda, K.; Thomas, A.; Takanabe, K.; Xin, G.; Carlsson, J.M.; Domen, K.; Antonietti, M. A metal-free polymeric photocatalyst for hydrogen production from water under visible light. *Nat. Mater.* **2009**, *8*, 76–80. [CrossRef] [PubMed]

19. Cai, Q.; Shen, J.; Feng, Y.; Shen, Q.; Yang, H. Template-free preparation and characterization of nanoporous g-C_3N_4 with enhanced visible photocatalytic activity. *J. Alloys Compd.* **2015**, *628*, 372–378. [CrossRef]

20. Shiraishi, Y.; Kanazawa, S.; Sugano, Y.; Tsukamoto, D.; Sakamoto, H.; Ichikawa, S.; Hirai, T. Highly selective production of hydrogen peroxide on graphitic carbon nitride (g-C_3N_4) photocatalyst activated by visible light. *ACS Catal.* **2014**, *4*, 774–780. [CrossRef]

21. Shiraishi, Y.; Kanazawa, S.; Kofuji, Y.; Sakamoto, H.; Ichikawa, S.; Tanaka, S.; Hirai, T. Sunlight-driven hydrogen peroxide production from water and molecular oxygen by metal-free photocatalysts. *Angew. Chem. Int. Ed.* **2014**, *53*, 13454–13459. [CrossRef] [PubMed]

22. Shiraishi, Y.; Kofuji, Y.; Sakamoto, H.; Tanaka, S.; Ichikawa, S.; Hirai, T. Effects of surface defects on photocatalytic H_2O_2 production by mesoporous graphitic carbon nitride under visible light irradiation. *ACS Catal.* **2015**, *5*, 3058–3066. [CrossRef]

23. Kofuji, Y.; Ohkita, S.; Shiraishi, Y.; Sakamoto, H.; Tanaka, S.; Ichikawa, S.; Hirai, T. Graphitic carbon nitride doped with biphenyl diimide: Efficient photocatalyst for hydrogen peroxide production from water and molecular oxygen by sunlight. *ACS Catal.* **2016**, *6*, 7021–7029. [CrossRef]

24. Kofuji, Y.; Isobe, Y.; Shiraishi, Y.; Sakamoto, H.; Tanaka, S.; Ichikawa, S.; Hirai, T. Carbon nitride-aromatic diimide-graphene nanohybrids: MetalFree photocatalysts for solar-to-hydrogen peroxide energy conversion with 0.2% efficiency. *J. Am. Chem. Soc.* **2016**, *138*, 10019–10025. [CrossRef] [PubMed]

25. Moon, G.-H.; Fujitsuka, M.; Kim, S.; Majima, T.; Wang, X.; Choi, W. Eco-Friendly photochemical production of H_2O_2 through O_2 reduction over carbon nitride frameworks incorporated with multiple heteroelements. *ACS Catal.* **2017**, *7*, 2886–2895. [CrossRef]

26.　Wang, R.; Pan, K.; Han, D.; Jiang, J.; Xiang, C.; Huang, Z.; Zhang, L.; Xiang, X. Solar-driven H_2O_2 generation from H_2O and O_2 using earth-abundant mixed-metal oxide@carbon nitride photocatalysts. *ChemSusChem* **2016**, *9*, 2470–2479. [CrossRef] [PubMed]

27.　Li, Y.; Zhang, L.; Xiang, X.; Yan, D.; Li, F. Engineering of ZnCo-layered double hydroxide nanowalls toward high-efficiency electrochemical water oxidation. *J. Mater. Chem. A* **2014**, *2*, 13250–13258. [CrossRef]

28.　Tang, Y.; Wang, R.; Yang, Y.; Yan, D.; Xiang, X. Highly enhanced photoelectrochemical water oxidation efficiency based on triadic quantum dot/layered double hydroxide/$BiVO_4$ photoanodes. *ACS Appl. Mater. Interfaces* **2016**, *8*, 19446–19455. [CrossRef] [PubMed]

29.　Han, D.; Liu, J.; Yang, J.; Xiang, X. In-situ conversion and catalytic properties of mixed-metal oxide catalysts for photosynthesis of hydrogen peroxide. *Sci. China-Chem.* **2017**, *47*, 465–473. [CrossRef]

30.　Wang, R.; Zhang, X.; Li, F.; Cao, D.; Pu, M.; Han, D.; Yang, J.; Xiang, X. Energy-level dependent H_2O_2 production on metal-free, carbon-content tunable carbon nitride photocatalysts. *J. Energy Chem.* **2018**, *27*, 343–350. [CrossRef]

31.　Tan, Y.; Liu, X.Y.; Zhang, L.; Wang, A.; Li, L.; Pan, X.; Miao, S.; Haruta, M.; Wei, H.; Wang, H.; et al. ZnAl-hydrotalcite-supported Au_{25} nanoclusters as precatalysts for chemoselective hydrogenation of 3-nitrostyrene. *Angew. Chem. Int. Ed.* **2017**, *56*, 2709–2713. [CrossRef] [PubMed]

32.　Zhan, W.; He, Q.; Liu, X.; Guo, Y.; Wang, Y.; Wang, L.; Guo, Y.; Borisevich, A.Y.; Zhang, J.; Lu, G.; et al. A sacrificial coating strategy toward enhancement of metal-support interaction for ultrastable Au nanocatalysts. *J. Am. Chem. Soc.* **2016**, *138*, 16130–16139. [CrossRef] [PubMed]

33.　Chen, J.; Shen, S.; Guo, P.; Wu, P.; Guo, L. Spatial engineering of photo-active sites on g-C_3N_4 for efficient solar hydrogen generation. *J. Mater. Chem. A* **2014**, *2*, 4605–4612. [CrossRef]

34.　Sun, X.; Dong, S.; Wang, E. Large-Scale synthesis of micrometer-scale single-crystalline Au plates of nanometer thickness by a wet-chemical route. *Angew. Chem. Int. Ed.* **2004**, *116*, 6520–6523. [CrossRef]

35.　Leff, D.V.; Brandt, L.; Heath, J.R. Synthesis and characterization of hydrophobic, organically-soluble gold nanocrystals functionalized with primary amines. *Langmuir* **1996**, *12*, 4723–4730. [CrossRef]

36.　Park, M.; Shin, K.S.; Lee, J.W.; Kim, K. Novel fabrication of Au nanoparticle film on a polyelectrolyte-coated glass for efficient surface-enhanced raman scattering. *Bull. Korean Chem. Soc.* **2015**, *36*, 743–747.

37.　Singh, J.A.; Overbury, S.H.; Dudney, N.J.; Li, M.; Veith, G.M. Gold nanoparticles supported on carbon nitride: Influence of surface hydroxyls on low temperature carbon monoxide oxidation. *ACS Catal.* **2012**, *2*, 1138–1146. [CrossRef]

38.　Kartusch, C.; Krumeich, F.; Safonova, O.; Hartfelder, U.; Makosch, M.; Sa, J.; Bokhoven, J.A. Redispersion of gold multiple-twinned particles during liquid-phase hydrogenation. *ACS Catal.* **2012**, *2*, 1394–1403. [CrossRef]

39.　Gao, L.F.; Wen, T.; Xu, J.Y.; Zhai, X.P.; Zhao, M.; Hu, G.W.; Chen, P.; Wang, Q.; Zhang, H.L. Iron-doped carbon nitride-type polymers as homogeneous organocatalysts for visible light-driven hydrogen evolution. *ACS Appl. Mater. Interfaces* **2016**, *8*, 617–624. [CrossRef] [PubMed]

40.　Khabashesku, V.N.; Zimmerman, J.L.; Margrave, J.L. Powder synthesis and characterization of amorphous carbon nitride. *Chem. Mater.* **2000**, *12*, 3264–3270. [CrossRef]

41.　Guo, Q.; Xie, Y.; Wang, X.; Lv, S.; Hou, T.; Liu, X. Characterization of well crystallized graphitic carbon nitride nanocrystallites via a benzene thermal route at low temperatures. *Chem. Phys. Lett.* **2003**, *380*, 84–87. [CrossRef]

42.　Guo, Q.; Yang, Q.; Zhu, L.; Yi, C.; Zhang, S.; Xie, Y. A facile one pot solvothermal route to tubular forms of luminescent polymeric networks $[(C_3N_3)_2(NH)_3]_n$. *Solid State Commun.* **2004**, *132*, 369–374. [CrossRef]

43.　Wang, S.; Li, C.; Wang, T.; Zhang, P.; Li, A.; Gong, J. Controllable synthesis of nanotube-type graphitic C_3N_4 and their visible-light photocatalytic and fluorescent properties. *J. Mater. Chem. A* **2014**, *2*, 2885–2890. [CrossRef]

44.　Zhan, G.; Huang, J.; Du, M.; Sun, D.; Abdul-Rauf, I.; Lin, W.; Hong, Y.; Li, Q. Liquid phase oxidation of benzyl alcohol to benzaldehyde with novel uncalcined bioreduction Au catalysts: High activity and durability. *Chem. Eng. J.* **2012**, *187*, 232–238. [CrossRef]

45.　Xu, Z.; Quintanilla, M.; Vetrone, F.; Govorov, A.O.; Chaker, M.; Ma, D. Harvesting lost photons: Plasmon and upconversion enhanced broadband photocatalytic activity in core@shell microspheres based on lanthanide-doped $NaYF_4$, TiO_2, and Au. *Adv. Funct. Mater.* **2015**, *25*, 2950–2960. [CrossRef]

46. Liu, J.; Liu, Y.; Liu, N.; Han, Y.; Zhang, X.; Huang, H.; Lifshitz, Y.; Lee, S.-T.; Zhong, J.; Kang, Z. Metal-free efficient photocatalyst for stable visible water splitting via a two-electron pathway. *Science* **2015**, *347*, 970–974. [CrossRef] [PubMed]

47. Moon, G.-H.; Kim, W.; Bokare, A.-D.; Sung, N.-H.; Choi, W. Solar production of H_2O_2 on reduced graphene oxide—TiO_2 hybrid photocatalysts consisting of earth-abundant elements only. *Energy Environ. Sci.* **2014**, *7*, 4023–4028. [CrossRef]

48. Chao, C.; Liu, J.; Wang, J.; Zhang, Y.; Zhang, B.; Zhang, Y.; Xiang, X.; Chen, R. Surface Modification of Halloysite Nanotubes with Dopamine for Enzyme Immobilization. *ACS Appl. Mater. Interfaces* **2013**, *5*, 10559–10564. [CrossRef] [PubMed]